Full-potential linear augmented–Slater-type-orbital method

G. W. Fernando, J. W. Davenport, R. E. Watson, and M. Weinert
Department of Physics, Brookhaven National Laboratory, Upton, New York 11973-6000
(Received 15 March 1989)

We have incorporated the full potential into the linear augmented–Slater-type-orbital method. Here we report on the details of the calculations and also specifically on the nature and the significance of the non-muffin-tin terms, some interesting structures of the potential and the charge density for standard test systems such as fcc Al, bcc W, fcc Pt, all of which have the O_h point-group symmetry. We have seen that for cubic systems, both the $l=4$ and $l=6$ components of the charge density and the potential in the sphere regions are important. We have also seen that this method with its inherently small basis set is capable of yielding total energies of comparable accuracy to the full-potential linear augmented-plane-wave method.

I. INTRODUCTION

First-principles electronic-structure calculations have come a long way during the last two decades. There is now a standard procedure, based on the Hohenberg-Kohn-Sham local-density approximation, which has been quite successful in predicting, for example, crystal structures, heat of formation, charge density contours, and surface states. This standard procedure involves the solution of the one-electron Schrödinger equation and the construction of the charge density by summing over occupied orbitals. There have been many techniques proposed for solving the Schrödinger equation but most of the modern ones used some sort of a basis set so that the problem is reduced to diagonalizing a matrix. The most common basis sets consist of plane waves or augmented plane waves which have been shown to be extremely accurate but also expensive since rather large matrices have to be constructed and diagonalized. Previously we have suggested using augmented Slater-type orbitals as a basis set—one which is significantly smaller so that diagonalization is not the rate-limiting step. However, the method was only set up for muffin-tin potentials. The purpose of this paper is to extend it to include the non-muffin-tin terms as well.

For systems with low symmetries, such as the $A15$ compounds, full potentials are certainly important. However, we will show here that even for highly symmetric cubic systems the full potential can have significant effects on certain quantities such as the t_{2g}-e_g splitting of the d bands at the center of the Brillouin zone. We will also show that the total potential along different crystal directions can vary by as much as 5–10 eV near the muffin-tin sphere boundaries in cubic crystals and that the charge densities deviate significantly from the muffin-tin behavior. Finally we will compare some of our calculated energies with other calculations and experiments.

II. METHOD

A. Basis set

The linear augmented-Slater-type-orbital (LASTO) basis set has been described in detail elsewhere.[1,2] Briefly, the crystal is partitioned into muffin-tin and interstitial regions. In the interstitial the basis is a Bloch sum of Slater-type orbitals,

$$\phi_{nlm}(\mathbf{r})=r^{n-1}\exp(-\zeta r)Y_{lm}(\hat{\mathbf{r}}) , \tag{1}$$

where the Y_{lm}'s are the usual spherical harmonics. Then

$$\psi_N(\mathbf{r})=\frac{1}{\sqrt{N_c}}\sum_{\mathbf{R}}\exp(i\mathbf{k}\cdot\mathbf{R})\phi_{nlm}(\mathbf{r}-\mathbf{R}-\tau_i) , \tag{2}$$

where $N:=\{i,n,lm,\}$, is a collective index, $\mathbf{R}$ labels a unit cell vector, τ_i the position of the ith atom within the unit cell, and N_c the total number of cells in the crystal.

The Slater-type orbitals have several desirable features such as having a nonsingular behavior everywhere in space and falling off as atomic wave functions at large distances. Their Fourier transforms can also be obtained analytically. From Refs. 1 and 2,

$$\tilde{\phi}_{nL}(\mathbf{q})=\frac{4\pi(-i)^l Y_L(\hat{\mathbf{q}})}{\Omega}\times\int_0^\infty dr\, j_l(qr)r^{n+1}\exp(-\zeta r) \tag{3}$$

is the Fourier transform of a Slater-type orbital with $\mathbf{q}=\mathbf{k}+\mathbf{G}$, $L:=\{l,m\}$ is a collective angular momentum index, and Ω is the volume of the unit cell. The integral appearing in the above equation can be evaluated analytically.[1] It consists of a ratio of two polynomials in q. Actually it is much more convenient to use the reciprocal-lattice representation of Eq. (2). It is straightforward to show that

$$\psi_N(\mathbf{r})=\frac{1}{\sqrt{N_c}}\sum_{\mathbf{q}}\exp[i\mathbf{q}\cdot(\mathbf{r}-\tau_i)]\tilde{\phi}_{nL}(\mathbf{q})=\sum_{\mathbf{q}}\exp(i\mathbf{q}\cdot\mathbf{r})\tilde{\psi}_N(\mathbf{q}) . \tag{4}$$

As with the other augmented schemes the basis function inside the jth sphere is taken to be

$$\psi_{inL}(\mathbf{r})=\sum_{\Lambda}[\beta_{inL,j\Lambda}g_{j\lambda}(r_j)+\alpha_{inL,j\Lambda}\dot{g}_{j\lambda}(r_j)]Y_\Lambda(\hat{\mathbf{r}}_j) , \tag{5}$$

where g and $\dot{g}$ are solutions of the scalar-relativistic Dirac equation and its energy derivative. The β's and α's are chosen by matching the interior and the exterior functions and their spatial derivatives at the sphere boundary. Here $\Lambda := \{\lambda,\mu\}$ denotes the angular momentum indices, and our cutoff value $\lambda_{\max}$ is 8.

Using these basis functions, we construct the overlap matrix

$$S_{NN'} = \int \psi_N^*(\mathbf{r})\psi_{N'}(\mathbf{r})d^3r$$

and the matrix elements of the muffin-tin part of the Hamiltonian $H_{NN'}^{\mathrm{MT}}$ may be evaluated as described previously.[2]

B. Non-muffin-tin matrix elements

As in the full-potential linear augmented-plane-wave (FLAPW) method[3–5] the total potential can be represented as a Fourier expansion in the interstitial region and as an expansion in spherical harmonics inside the spheres. Therefore, in the interstitial

$$V(\mathbf{r}) = \sum_{\mathbf{G}} \exp(i\mathbf{G}\cdot\mathbf{r})\tilde{V}(\mathbf{G}) , \tag{6}$$

while inside the jth sphere it has the form

$$V^j(\mathbf{r}) = \sum_{\nu} V_\nu^j(r_j)K_{l_\nu}(\hat{\mathbf{r}}_j) , \tag{7}$$

where the K_{l_ν}'s are the normalized lattice harmonics which have the full local symmetry about the jth atom site. From these expressions the non-muffin-tin (NMT) matrix elements of the Hamiltonian

$$H_{NN'} = \int \psi_N^* V(\mathbf{r})\psi_{N'}\, d^3r \tag{8}$$

can be constructed. For the jth sphere, the NMT parts of the matrix elements are given by

$$H_{NN'}^{\mathrm{sphere}} = \sum_{\Lambda,\Lambda',\nu} \int K_\nu Y_\Lambda^* Y_{\Lambda'}\, d\hat{\mathbf{r}} \left[\beta_{N,j\Lambda}^*\beta_{N',j\Lambda'}\int g_{j\lambda}V_\nu^j g_{j\lambda'}r^2\,dr + \beta_{N,j\Lambda}^*\alpha_{N',j\Lambda'}\int g_{j\lambda}V_\nu^j \dot{g}_{j\lambda'}r^2\,dr \right.$$
$$\left. + \alpha_{N,j\Lambda}^*\beta_{N',j\Lambda'}\int \dot{g}_{j\lambda}V_\nu^j g_{j\lambda'}r^2\,dr + \alpha_{N,j\Lambda}^*\alpha_{N',j\Lambda'}\int \dot{g}_{j\lambda}V_\nu^j \dot{g}_{j\lambda'}r^2\,dr \right] . \tag{9}$$

Although these may seem to involve many indices and hence be computationally cumbersome they can be handled efficiently using the properties of the Gaunt integrals (integral of the product of three spherical harmonics). For a highly symmetric system the number of nonvanishing Gaunt coefficients can be quite small. These Gaunt integrals are done using a Gaussian integration technique.

For an atom with local cubic symmetry, the normalized, nonzero lattice harmonics up to $l=8$ entering Eq. (7) are given by

$$K_0 = Y_{0,0} ,$$
$$K_4 = \sqrt{\tfrac{7}{12}}Y_{4,0} + \sqrt{\tfrac{5}{24}}(Y_{4,-4}+Y_{4,4}) ,$$
$$K_6 = \frac{\sqrt{2}}{4}Y_{6,0} - \frac{\sqrt{7}}{4}(Y_{6,-4}+Y_{6,4}) ,$$
$$K_8 = \frac{\sqrt{33}}{8}Y_{8,0} + \tfrac{1}{8}\sqrt{\tfrac{14}{3}}(Y_{8,-4}+Y_{8,4}) + \tfrac{1}{24}\sqrt{\tfrac{195}{2}}(Y_{8,-8}+Y_{8,8}) .$$

The interstitial contribution to the Hamiltonian matrix elements is handled via the step function θ defined as

$$\theta(\mathbf{r}) = \begin{cases} 1, & \mathbf{r}\in\text{interstitial region;} \\ 0, & \text{otherwise.} \end{cases} \tag{10}$$

The Fourier transform of the step function θ is

$$\tilde{\theta}(\mathbf{G}) = \delta_{\mathbf{G},0} - \frac{4\pi}{\Omega}\sum_{\gamma}\frac{\exp(-i\mathbf{G}\cdot\mathbf{R}_\gamma)R_\gamma^3 j_1(GR_\gamma)}{GR_\gamma} , \tag{11}$$

where R_γ denotes the radius of the sphere γ. The contribution to the Hamiltonian matrix is obtained as

$$H_{NN'}^{\mathrm{interstitial}} = \Omega\sum_{\mathbf{G}}\tilde{\psi}_N^*(\mathbf{q})\sum_{\mathbf{G}'}\tilde{f}(\mathbf{G}-\mathbf{G}')\tilde{\psi}_{N'}(\mathbf{q}') , \tag{12}$$

where $\tilde{f}$ is the Fourier transform of the product

$$f(\mathbf{r}) = V(\mathbf{r})\theta(\mathbf{r}) . \tag{13}$$

Although the step functions θ and f have slowly converging Fourier expansions due to their discontinuities, it does not affect the accuracy of the matrix elements defined by Eq. (12). This is due to the cutoff in the Fourier expansion of the basis function $\tilde{\psi}_N$ which determines the accuracy of Eq. (12). We use fast Fourier transforms (FFT) to handle the product function. The Fourier series cutoff for the potential and the charge density is chosen to be twice that of the basis functions. This will guarantee that when taking products of the form $\psi^*\psi$ we do not throw away the extremum contributions. Also note that the overlap contribution to the matrix element is obtained easily by replacing $\tilde{f}$ by $\tilde{\theta}$.

The resulting Hamiltonian (H) and overlap (S) matrices lead to the secular equation

$$\sum_{N'} H_{NN'}A_{N'} = \epsilon\sum_{N'} S_{NN'}A_{N'} . \tag{14}$$

C. Charge density

Once the above eigenvalue problem is solved the charge density can be constructed by summing over the occupied states I as

$$\rho(\mathbf{r}) = \sum_{\mathbf{k},I} \Psi_{\mathbf{k}}^{I*}\Psi_{\mathbf{k}}^{I} , \tag{15}$$

where

$$\Psi_{\mathbf{k}}^{I}(\mathbf{r})=\sum_{N} A_N^I \psi_N(\mathbf{r}) .$$

The sum in Eq. (15) should be carried out over the full Brillouin zone (BZ). In practice one wishes to work in an irreducible wedge of the BZ (IBZ) which for cubic systems is $\frac{1}{48}$ as large. The Hamiltonian is invariant under all 48 symmetry operations and therefore the eigenvalues are the same no matter which irreducible wedge is chosen. However the charge density is not so behaved and therefore the density obtained from $\frac{1}{48}$ of the zone does not necessarily have the full symmetry of the lattice. To obtain the properly symmetrized density it is necessary to relate the Bloch functions in different wedges of the Brillouin zone. This may be done using the space-group operators.

$$S=\{R\,|\mathbf{t}\} , \tag{16}$$

where R is a rotation and $\mathbf{t}$ a translation.

The effect of S on a Bloch function $\psi_{\mathbf{k}}(\mathbf{r})$ is to produce a Bloch function with $\mathbf{k}'=R\mathbf{k}$. But the set of all $R\mathbf{k}$ spans the entire Brillouin zone. Therefore

$$\sum_{\mathrm{BZ}} \psi_{\mathbf{k}}^{*}(\mathbf{r})\psi_{\mathbf{k}}(\mathbf{r})=\sum_{\substack{\mathbf{k}\in\mathrm{IBZ}\\ S}} [S\psi_{\mathbf{k}}(\mathbf{r})]^{*}S\psi_{\mathbf{k}}(\mathbf{r}) . \tag{17}$$

Further, this density has the full symmetry of the lattice because the sum on S on the right-hand side of Eq. (17) is a projection operator which projects out the part of $\psi_{\mathbf{k}}^{*}\psi_{\mathbf{k}}$ which transforms according to the fully symmetric representation of the space group. Now by definition

$$S\psi_{\mathbf{k}}(\mathbf{r})=\psi_{\mathbf{k}}(S^{-1}\mathbf{r}) \tag{18}$$

so

$$\rho(\mathbf{r})=\frac{1}{n_0}\sum_{S,\,\mathrm{occupied}} \Psi_{\mathbf{k}}^{I\,*}(S^{-1}\mathbf{r})\Psi_{\mathbf{k}}^{I}(S^{-1}\mathbf{r}) . \tag{19}$$

The symmetrized charge density in the jth sphere may also be written as

$$\rho^{j}(\mathbf{r})=\sum \rho_{\nu}^{j}(r_j)K_{l_\nu}(\hat{\mathbf{r}}_j) \tag{20}$$

Using Eqs. (19) and (20) it is possible to obtain ρ_{ν}^{j} which will completely determine the charge density in the spheres.

The interstitial density is calculated as follows. If A_N^I denotes the coefficients of the eigenstate I, then define

$$\tilde{B}^{I}(\mathbf{q})=\sum_{N} A_N^I \tilde{\psi}_N(\mathbf{q}) . \tag{21}$$

If $B^I(\mathbf{r})$ is the inverse Fourier transform of $\tilde{B}^{I}(\mathbf{q})$, then the summation

$$\sum_{\mathrm{occupied}} B^{I\,*}(\mathbf{r})B^{I}(\mathbf{r})$$

will give rise to an unsymmetrized density. By Fourier transforming this density and symmetrizing according to the symmetry of the space group of the problem, as discussed above, the complete (plane-wave) density $\tilde{\rho}_{\mathrm{pw}}(\mathbf{G})$ in the interstitial regions may be found.

D. Potential

As noted previously the form of the crystal potential is given by Eq. (7) in the sphere regions while the interstitial potential is given in terms of a Fourier expansion [Eq. (6)]. There are two separate contributions to the potential, namely the exchange-correlation and the Coulomb potential. In order to calculate the Coulomb potential it is necessary to solve Poisson's equation. The strategy, suggested by Weinert[6] and Hamann,[4] is to first calculate the potential in the interstitial region by replacing the actual charge density inside the spheres with a smoothly varying pseudodensity having the same multipole moments. This will determine the potential everywhere in the interstitial including the sphere boundaries. Then the potential inside the spheres can be obtained by solving a boundary value problem with the true density. The need for a pseudodensity arises from the fact that a Fourier expansion of the true density would require an impossibly large number of Fourier components because of the rapid variation of the charge density near the nuclei.

Following Weinert[6] we would like the pseudodensity to have the following properties. (a) It should have the same multipole moments as the difference, *true density–plane-wave density,* inside the spheres. (b) It should go smoothly to zero at the sphere boundaries $r=R$. (c) Its Fourier transform should be known analytically.

It turns out that the following radial function can be used to construct a pseudodensity satisfing the above requirements:[6]

$$n_{lm}^{\mathrm{pseudo}}(r)=a_{lm}(r/R)^{l}[1-(r/R)^2]^{n}, \quad r\le R . \tag{22}$$

Here a_{lm} should be chosen to have the correct multipole moment and n is arbitrary. The larger n, the more derivatives of the pseudodensity vanish at the sphere boundaries. Different values of n can be chosen for different atoms and different angular momenta to optimize convergence. We have used n values as high as 14 in the calculations reported here. This radial form combined with the correct angular dependence (Y_{lm}) plus the plane-wave density [$\tilde{\rho}_{\mathrm{pw}}(\mathbf{G})$] gives rise to the total pseudodensity,

$$\tilde{\rho}^{\,\mathrm{pseudo}}(\mathbf{G})=\tilde{n}(\mathbf{G})+\tilde{\rho}_{\mathrm{pw}}(\mathbf{G}) . \tag{23}$$

Solving the Poisson equation for this density yields the correct Coulomb potential in the interstitial region, i.e.,

$$\tilde{V}^{\,\mathrm{Coulomb}}(\mathbf{G})=\frac{4\pi\tilde{\rho}^{\,\mathrm{pseudo}}(\mathbf{G})}{\mathbf{G}^2}, \quad \mathbf{G}\neq\mathbf{0} . \tag{24}$$

The choice of the zero of the potential is arbitrary, and we choose it to be the average of the interstitial Coulomb potential.

In the sphere regions, calculating the Coulomb potential is equivalent to solving a standard Dirichlet's problem since the potential at the sphere boundaries is known.[3–6] For completeness we show the expression for the Coulomb potential inside a sphere of radius R below (for $l_\nu=0$, ρ_{l_ν} includes the nuclear charge density also),

$$V_{l_v}(r)=\frac{4\pi}{2l+1}\left[\frac{1}{r^{l_v+1}}\int_0^r (r')^{l_v+2}\rho_{l_v}\,dr'+r^{l_v}\int_r^R (r')^{1-l}\rho_{l_v}\,dr'\right]$$
$$+\left[\frac{r}{R}\right]^{l_v}\left[V_{l_v}^{\text{Coulomb}}(R)-\frac{4\pi}{(2l+1)R^{l_v+1}}\int_0^R (r')^{l_v+2}\rho_{l_v}\,dr'\right], \quad (25)$$

where the Coulomb potential on the sphere boundary is given by

$$V_{l_v}^{\text{Coulomb}}(R)=4\pi i^{l_v}\sum_{\mathbf{G}}\tilde{V}^{\text{Coulomb}}(\mathbf{G})K_{l_v}^*(\hat{\mathbf{G}})$$
$$\times j_{l_v}(GR)\exp(i\mathbf{G}\cdot\tau_i)\ . \quad (26)$$

Note that the potential in Eq. (25) is the sum of the well-known volume term and a surface contribution.

To calculate the exchange-correlation potential at a given point in space it is necessary to obtain the charge density there. The charge density is easily found from the methods described previously. The exchange-correlation potential in the sphere regions is obtained using a Gaussian set of points in the unit sphere with corresponding weights. This set of 150 points integrates products of spherical harmonics $Y_L^* Y_{L'}$ to machine accuracy for $l,l'\leq 9$. The starburst mesh mentioned in Ref. 4 fails for such products at l values such as 8. Since our l expansion goes up to $l=8$, we have used the Gaussian mesh in the present calculations.

The exchange-correlation potential in the interstitial regions is handled with an FFT algorithm. The Fourier coefficients of the density calculated above are used to get the real-space density and hence the exchange-correlation potential. We have used the Hedin-Lundqvist[7] form in the calculations reported here.

III. RESULTS

A. Computational details

In order to test the full-potential LASTO method we have calculated the charge densities, potentials, total energies of bcc tungsten, fcc platinum, and fcc aluminum.

We varied the basis set from single ζ (1ζ) which includes $5d$, $6s$, and $6p$ for W and Pt, and $3s$ and $3p$ for Al to double ζ (2ζ) which adds $6d$, $7s$, and $7p$ for W and Pt and $4s$ and $4p$ for Al to double $\zeta+$ polarization term which adds a $4f$ function to W and Pt and a $3d$ function to Al. The ζ values are listed in Table I. They were chosen to minimize the total energy of the metal in its normal crystal structure.

The wave function inside the spheres in Eq. (5) was carried up to $\lambda=8$ as were the charge density and the potential. In the interstitial, the reciprocal-lattice expansion was carried up to a cutoff of about $7a_0^{-1}$ for the density and the potential. The Brillouin zone was sampled at 110 special $\mathbf{k}$ points for the fcc structures and at 70 special $\mathbf{k}$ points for the bcc structure. The core levels were calculated self-consistently using the fully relativistic Dirac equation with the spherically symmetric part of the full potential.

In local-orbital methods such as LASTO and LMTO (linear muffin-tin-orbital method), a major fraction of the computer time is spent on constructing the matrix elements, while in the LAPW method the diagonalization step is the bottle neck. For small unit cells these methods may take comparable computer times with the local orbital methods being slightly faster. However, for large unit cells (with more than 10 atoms), the computer time for the diagonalization step, which increases as N_G^3 where N_G is the number of plane waves for the LAPW basis, is bound to slow down this method compared to a local orbital method. This is because the matrix element construction in a local basis method increases only as $N_L^2 N_G + N_G^2 N_L$ with N_G again being the number of plane waves used to expand the interstitial basis functions and N_L being the number of basis functions. Note that N_L is always very much smaller than N_G and for large unit cells we expect a gain of about N_G/N_L with LASTO compared to LAPW.

B. bcc W

The higher harmonics of the nonspherical density and the potential ρ_{l_v} and V_{l_v} for bcc W are shown in Figs. 1 and 2. It is clear from these figures that the $l=4$ and $l=6$ terms are the dominant nonspherical contributions to the potential and the charge density. We also note

TABLE I. Values of ζ for bcc W, fcc Pt, and fcc Al. LASTO parameter ζ in units of a_0^{-1} used in the calculations reported here. The orbital type (principal quantum number and the orbital angular momentum) is given in parentheses.

	bcc W	fcc Pt	fcc Al
Single ζ	(5*d*) 2.45	(5*d*) 2.65	(3*s*) 0.80
	(6*s*) 2.32	(6*s*) 2.66	(3*p*) 0.80
	(6*p*) 1.73	(6*p*) 1.96	
Double ζ+polarization	(6*d*) 4.03	(6*d*) 3.72	(4*s*) 1.00
	(7*s*) 1.90	(7*s*) 1.94	(4*p*) 1.00
	(7*p*) 2.73	(7*p*) 2.66	(3*d*) 1.20
	(5*f*) 1.38	(5*f*) 1.50	

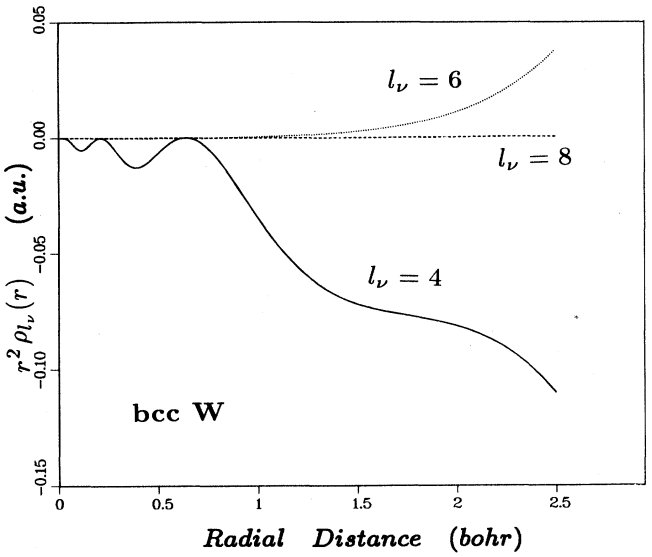

FIG. 1. The higher ($l=4,6,8$) harmonics of the density for bcc W. Note that the $l=4$ component follows the nodal structure of the 5*d* orbital.

that the $l=4$ term is non-negligible well inside the muffin-tin sphere. Note that for bcc W, the number of nodes in ρ_4 corresponds exactly to the number of nodes in the 5*d* orbital which will be explained later using Eq. (27). These harmonics can be used to generate the potential and the charge density inside the spheres, along an arbitrary direction in the crystal [using Eqs. (7) and (20)].

Shown in Figs. 3 and 4 are the charge density and the potential along (100), (110), and (111) directions near and outside the muffin-tin boundary. It is interesting to see the continuity of the potential and the charge density and their first derivatives at the sphere boundary since we have used two different representations in the two regions, sphere and interstitial. This clearly shows the adequacy of the cutoffs used in the various expansions in our calculations.

For the bcc structure, the (111) direction has the highest density since this is the direction of the bond with

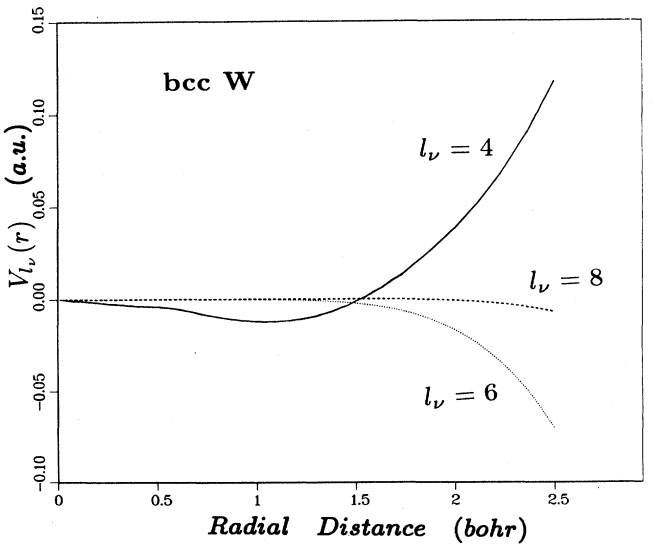

FIG. 2. The higher harmonics of the potential for bcc W in hartrees. Note that $l=4$ and $l=6$ components are comparable and significant near the sphere boundary.

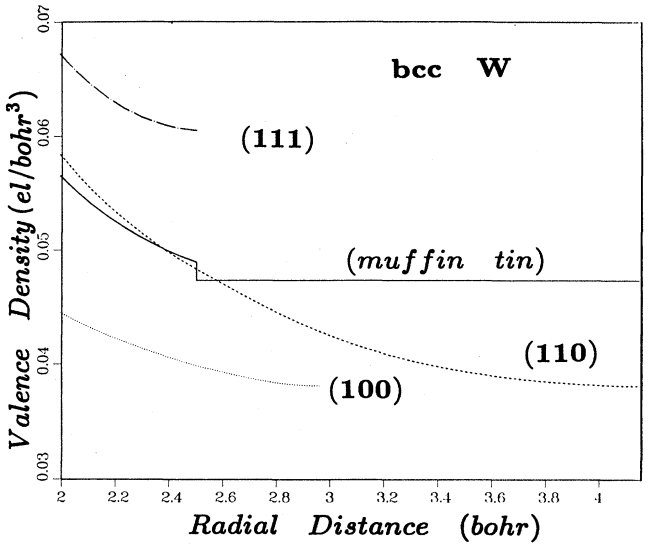

FIG. 3. The actual density along (111), (110), and (100) crystal directions for bcc W near and away from the sphere boundary. These have been shown up to the halfway point between neighboring atoms along a given direction. Although we have used two different representations for the density in the spheres and in the interstitial regions, note the continuity of these densities and their first derivatives with the full potential. The sphere boundary is at the point where there is a step discontinuity in the muffin-tin density.

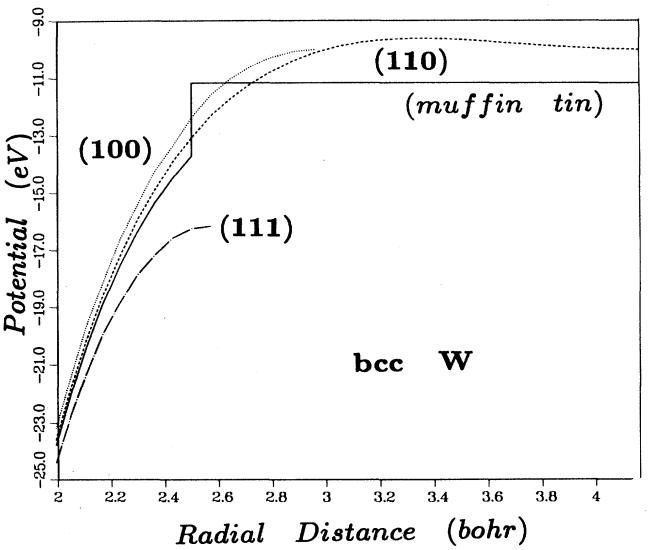

FIG. 4. The actual potential in eV along (111), (110), and (100) bcc W. These have been shown up to the halfway point between neighboring atoms along a given direction. The muffin-tin potential is also shown here for comparison, by aligning the 1*s* core level with the full-potential calculation.

the nearest neighbor. The next-highest density is along (110) in spite of the fact that the next-nearest neighbor is along (100). This most likely to be due to the stronger influence of the body centered atom. The potential along the above three directions follows the trends seen in the density; i.e., more negative potentials (hence more attractive) corresponding to higher charge densities. This is presumably due to the dominance of the exchange and correlation parts of the potential as compared to the Coulomb part. Also note that there is a weak minimum in the potential along (110) at the halfway point to the next atom.

It is also interesting to compare these to the results from a fully self-consistent muffin-tin calculation. As expected the muffin-tin potential and the density represent averages along these three directions near the muffin-tin sphere boundary. However note that out in the interstitial [for example, along (110)] the difference between the muffin-tin potential and the full potential can be as large as 2–3 eV. This shows that the muffin-tin potential is not a suitable approximation for open structures.

We have also looked at the t_{2g}-e_g splitting of the tungsten d bands at the center of the Brillouin zone with and without the full potential. The full-potential number, which is about 3.5 eV, agrees well with other tungsten calculations[5] and is about 0.5 eV larger than the value given by our muffin-tin calculation.

C. fcc Pt

The higher harmonics of the nonspherical density and the potential for fcc Pt are shown in Figs. 5 and 6. Again the $l=4$ and $l=6$ terms appear to be the most important. Note that they are of nearly equal magnitude at the sphere boundary and the $l=4$ terms are significant well inside the sphere boundary. It is important to have the $l=8$ terms at least as a check on the convergence of the

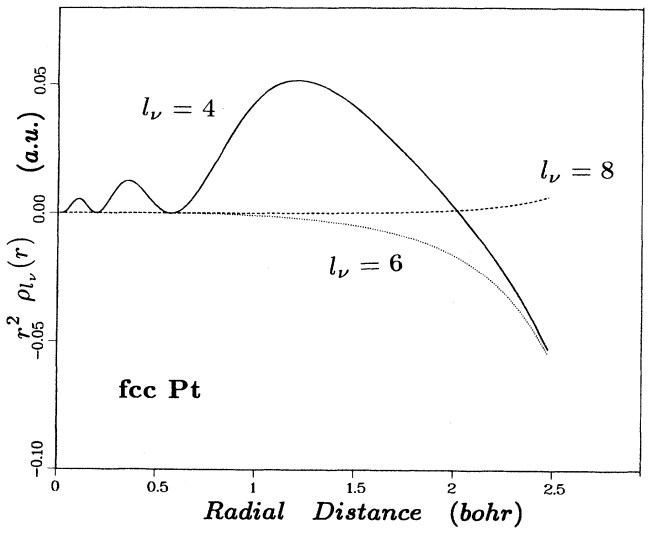

FIG. 5. The higher ($l=4,6,8$) harmonics of the density for fcc Pt. Again the nodal structure of the $l=4$ component is the same as that of the $5d$ function up to about $2a_0$. See text for various other conclusions that can be drawn from this figure.

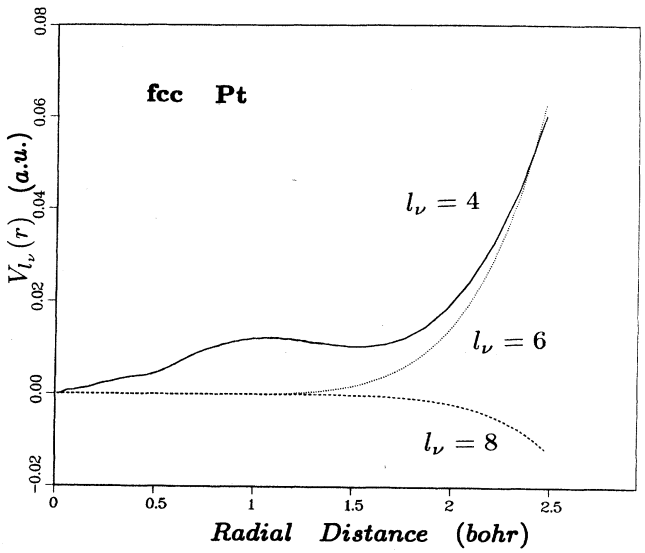

FIG. 6. The higher harmonics of the potential for fcc Pt in hartrees.

lattice harmonic expansion. For low-symmetry systems one may not be able to ignore the higher-l terms as we see here that for high-symmetry (cubic) systems one should at least go as high as $l=6$ in the lattice harmonic expansion inside the sphere regions. We also note that the $l=4$ and the $l=6$ harmonics of the calculated (fcc Pt) density closely resemble those reported in Ref. 8.

It is interesting to note that the $l=4$ and $l=6$ harmonics of fcc Pt have the opposite sign compared to those of bcc W up to a distance of about $2a_0$ from the nucleus. Most of the $l=6$ contribution is due to tails from the other sites. However, we may try to analyze this difference in sign of the $l=4$ harmonic in terms of the on

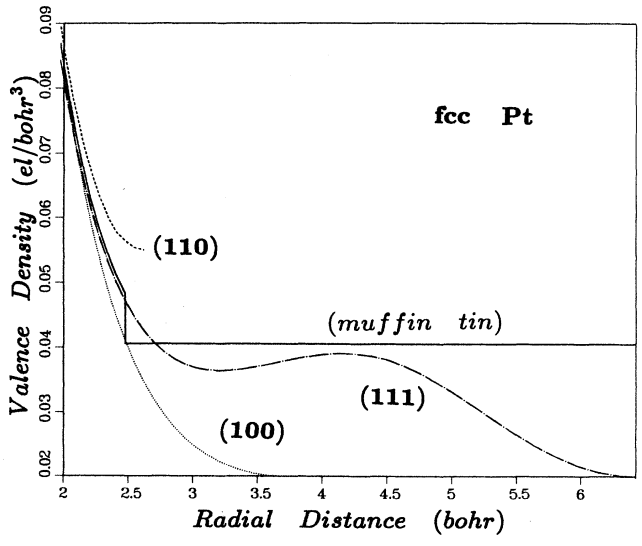

FIG. 7. The actual density along (111), (110), and (100) crystal directions for fcc Pt near and away from the sphere boundary. These have been shown up to the halfway point between neighboring atoms along a specified direction.

site d orbitals. If we carry out a rather simple analysis of ρ_4 in terms of the (non-negative) weights $w_{d_{x^2-y^2}}$ and $w_{d_{xy}}$ of the $d_{x^2-y^2}$ and d_{xy} orbitals (using an expansion of the wave function up to $l=2$), it can be shown that

$$\rho_4(r)=|g_2(r)|^2(w_{d_{x^2-y^2}}-w_{d_{xy}}) , \tag{27}$$

where $|g_2(r)|^2$ is a product of the square of the $l=2$ radial function, the relevant Gaunt integrals of the form $\int Y_{2,2}Y_{2,2}Y^*_{4,4}\,d\hat{\mathbf{r}}$ and other positive constants. This equation clearly explains why ρ_4 has the same nodal structure as the $5d$ function well inside the sphere. From Eq. (27) and Figs. 1 and 5, it is also clear that for bcc W, the dominant orbitals are t_{2g} (d_{xy}) type while for fcc Pt they are e_g ($d_{x^2-y^2}$). We may also roughly estimate (by comparing the magnitudes of ρ_4 and ρ_0) that these differences in orbital weights in Eq. (27) correspond to a few percent of the total charge density. While for bcc W the $l=4$ density harmonic does not change sign up to the muffin-tin sphere boundary, for fcc Pt it changes sign indicating the breakdown of the assumptions that led to Eq. (27), i.e., the importance of the higher-l orbitals near the sphere boundary.

The actual potential and the charge density are, of course, calculated by combining the above harmonics with the appropriate lattice harmonics as mentioned previously. In Figs. 7 and 8 we show these along the three crystal directions (100), (110), and (111) near and outside the sphere boundaries. The bond direction in the fcc structure is (110) and along this direction we see the highest valence density and the most negative (hence attractive) potential near the sphere boundary. Again we see the crystal potentials along these three directions differing by as much as 3 or 4 eV near the muffin-tin boundary. There are similar variations with respect to the muffin-tin potential as well.

There is a very interesting feature in the potential along the (111) direction which, to our knowledge has not been reported previously. The potential shows a double-well structure in the interstitial along this direction and the two minima (approximately) correspond to a $\frac{1}{3}$ and a $\frac{2}{3}$ of the distance between the two neighboring atoms along (111). There are, of course, the empty lattice sites of the fcc (111) stacking. It may be possible to trap light atoms like hydrogen in such potential wells. Further examination of the potential around this empty site shows that it is actually a saddle point. Anyway, this shows that the full potential scheme yields important information with regard to the structure of the density and the potential that cannot be obtained using other approximate methods and the above information may turn out to be crucial in situations such as interstitial trapping.

We also note here that the potentials again follow the charge densities (or vice versa) along these three crystal directions, i.e., more negative potentials correspond to higher charge densities. The t_{2g}-e_g splittings at the center of the Brillouin zone calculated from the self-consistent full-potential scheme and from the muffin-tin potential are about 2.2 and 2.0 eV, respectively. Although this difference in fcc Pt (0.2 eV) is not as large as

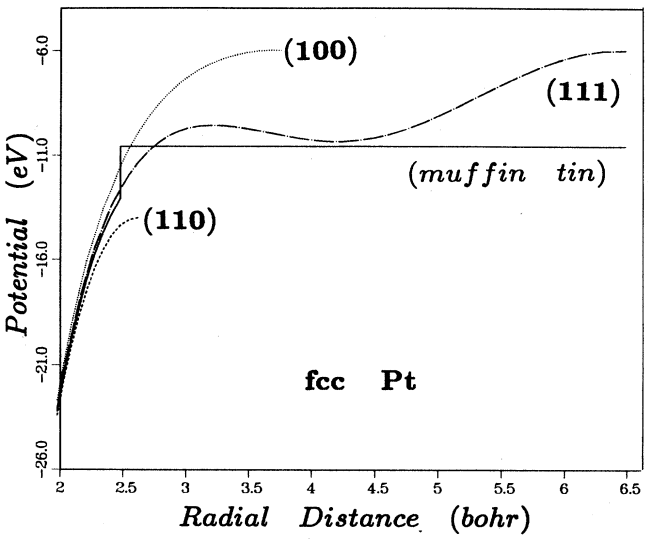

FIG. 8. The actual potential in eV along (111), (110), and (100) for fcc Pt. These have been shown up to the halfway point between neighboring atoms along a specified direction. Note the potential well along the (111) direction in the interstitial with a minimum at $\frac{1}{3}$ of the distance to the neighboring atom. There will be a similar minimum at the $\frac{2}{3}$ point giving rise to a double-well structure. Further examination of these features shows that these are saddle points.

that is calculated for bcc W (0.5 eV), it is still significant. The muffin-tin potential (and the density) once again represents an average potential (density) near the sphere boundary, but not in the far away interstitial regions, again showing its inadequacy in handling open structures.

D. fcc Al

Aluminum is thought to behave as a free-electron metal and hence it would be interesting to look for deviations

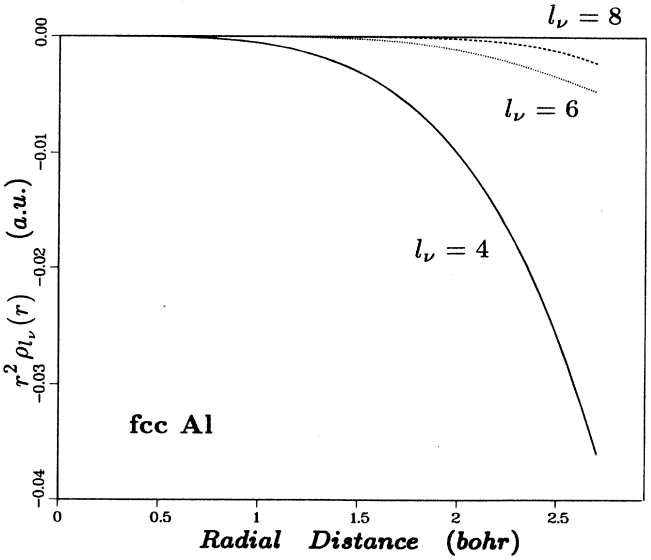

FIG. 9. The higher ($l=4,6,8$) harmonics of the density for fcc Al. Here the nodal structure of the $l=4$ component follows that of a $3d$ orbital (i.e., no nodes).

from that behavior, if any. The higher harmonics (Figs. 9 and 10) of the density and the potential are monotonic functions unlike in the cases of bcc W and fcc Pt. The spatial variations of these harmonics are definitely less than those of bcc W but somewhat comparable to fcc Pt in magnitude. Again the $l=4$ and the $l=6$ terms appear to be the most important. Once again we see that ρ_4 follows the nodal structure (zero nodes) of the $3d$ orbital which is the relevant one here and is mainly due to tails from the other sites.

The variations of the actual density and the potential along (100), (110), and (111) crystal directions are shown in Figs. 11 and 12. The densities along these three directions look somewhat flatter compared to the previous cases, however again there are variations of the order of a few eV in the potential along the three directions. We also note a double-well potential in the interstitial region along (111) similar to that seen in fcc Pt. Here also the two minima correspond to the $\frac{1}{3}$ and $\frac{2}{3}$ of the distance between neighboring atoms along the (111) direction. As explained for fcc Pt this is closely related to the fcc (111) stacking and should be expected in other fcc metals.

One important difference seen here from bcc W and fcc Pt is that the potentials along the three directions do not follow the trends in the charge densities. The bond direction, which is (110) for the fcc structure does not have the highest charge density near the sphere boundary, although it has the most negative (hence most attractive) potential in this region. The ordering (by magnitude) of the densities along (111) and (110) directions appear to have switched compared to what is seen for fcc Pt. This may be due to the different types of orbitals that contribute to the densities in this region for the two cases fcc Pt (d orbitals) and fcc Al (s and p orbitals) and its effects on the crystal field.

E. Total energies

In this section we will concentrate on total energies for the three test cases at hand. The total energy which is determined variationally can be extremely sensitive to various numerical cutoffs, choices of parameters (basis), sphere radii, etc. A well-converged total energy should not be sensitive to the above. Here we will show the degree of sensitivity of the total energy to our LASTO basis and for fcc Pt to the choice of the sphere radius.

Within the local-density approximation (LDA) the total energy may be written in the following convenient form:[9]

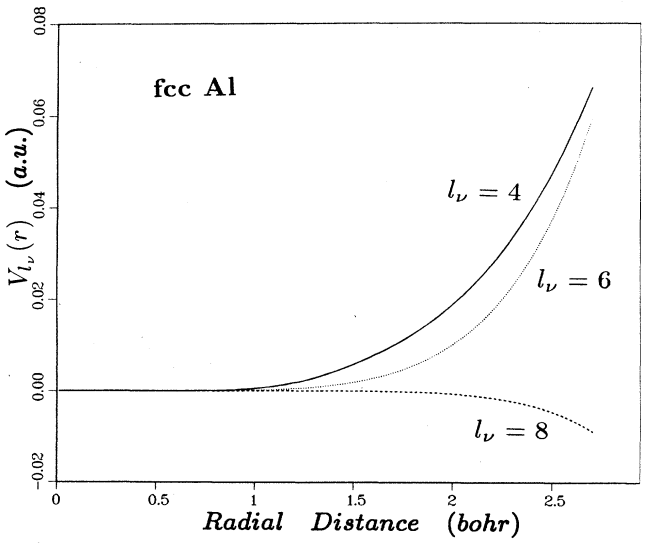

FIG. 10. The higher harmonics of the potential for fcc Al in hartrees.

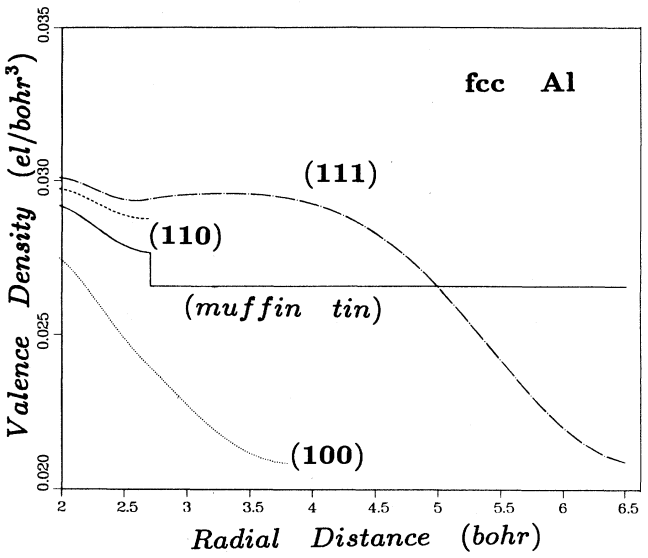

FIG. 11. The actual density along (111), (110), and (100) crystal directions for fcc Al near and away from the sphere boundary. These have been shown up to the halfway point between neighboring atoms along a specified direction.

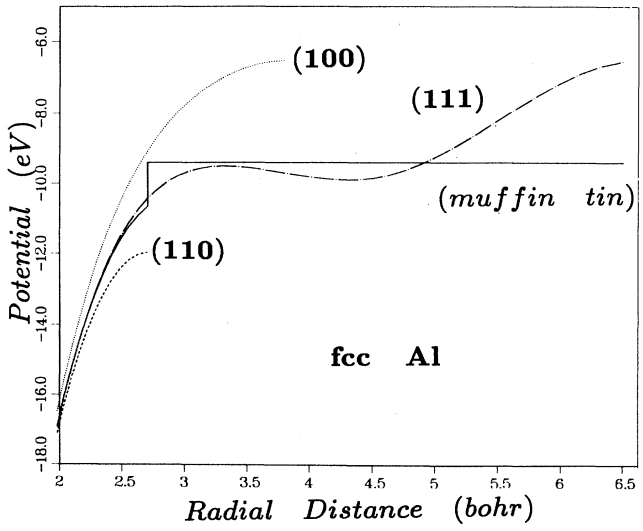

FIG. 12. The actual potential in eV along (111), (110), and (100) crystal directions for fcc Al near and away from the sphere boundary. These have been shown up to the halfway point between neighboring atoms along a specified direction. Note the potential well in the interstitial along (111) as in fcc Pt and the deviations from the muffin-tin behavior.

$$E[\rho]=\sum_i \epsilon_i-\tfrac{1}{2}\int_\Omega d\mathbf{r}\,\rho(\mathbf{r})\{V^{\text{Coulomb}}(\mathbf{r})+2[\mu^{\text{xc}}(\mathbf{r})-\varepsilon^{\text{xc}}(\mathbf{r})]\}$$
$$-\tfrac{1}{2}\sum_j Z_j\left[V^{\text{Coulomb}}(R_j)+\frac{1}{R_j}\left[Z_j-4\pi\int_0^{R_j}dr\,r^2\rho(r)\right]+4\pi\int_0^{R_j}dr\,r\rho(r)\right]. \quad (28)$$

Note that $\rho(\mathbf{r})$ $[V^{\text{Coulomb}}(\mathbf{r})]$ denotes the total density (Coulomb potential) while $\rho(r)$ $[V^{\text{Coulomb}}(R_j)]$ denotes the spherically averaged density (Coulomb potential) in a given sphere. Z_j refers to the nuclear charge and R_j the radius of the jth sphere in the unit cell.

Although the lattice constants can be calculated within our calculated scheme we have used experimental lattice constants (see Table II) for our test cases. However we have seen that our method is capable of predicting lattice constants to the same accuracy of the FLAPW method, and these results will be reported elsewhere.[10] The purpose of this section is to discuss the sensitivity of our total energies with respect to the choice of our LASTO parameters, sphere radius, and compare some of our results with other published work.

In Table I we show the LASTO parameters that were used in these calculations. These were chosen to minimize the total energies at the end of the self-consistent iterative process. Due to the finite basis that is used in these methods there is always a basis set error associated with the total energies. by adding more basis functions (double ζ+polarization) it is possible to reduce this error. For the muffin-tin calculations there is an additional error due to the shape approximations to the potential and the charge density.

Our total energies contain the contributions from the core as we recalculate the core self-consistently. However there remains the question of the semicore states such as the $5p$ states in W. Since these have a nonnegligible weight in the interstitial region, the correct way to calculate these is to treat them as valence states in a separate energy window. In the bcc W calculations reported here the $5p$ states have been treated as core states and the leakage into the interstitial has been treated approximately. However we intend to calculate them correctly as semicore in the future. We note that our total energy shows changes of the order of 8 or 9 mhartrees when going from a single-ζ basis to a double-ζ basis. The difference in our total energy with the full basis (double ζ+polarization), compared to the FLAPW calculation of Ref. 5 is mainly due to the different values used for the fine-structure constant as explained in Ref. 2.

In fcc Pt the core leakage is much smaller than in bcc W. With the full basis, the total energy is not sensitive to the change in sphere radius from $2.477a_0$ to $2.62a_0$ showing the adequacy of the basis and also other cutoffs used in our calculations. Corresponding to the above change in the sphere radius, the muffin-tin potential, single-ζ basis total energy changes by 12 millihartrees while the full-potential, single-ζ basis total energy changes by 4 millihartrees. This sensitivity in the full-potential case is an indication of the basis set error, which gets much smaller with the full (double ζ+polarization) basis. It appears that in this improvement to the single-ζ basis, the $5f$ function is more important than the $6d$'s and the rest.

For fcc Pt, as well as fcc Al, the total energy changes only by two-tenths of a millihartree corresponding to a 5–7 % change in the sphere radius with the full basis. This is another indication of the adequacy of the basis set as well as the accuracy of our full-potential scheme. All the total energies reported here have been calculated using 110 (fcc) or 70 (bcc) special k points in the corresponding irreducible wedge of the Brillouin zone.

TABLE II. Total energies for bcc W, fcc Pt, and fcc Al. Self-consistently calculated total energies in hartrees for ζ values given in Table I, for bcc W, fcc Pt, and fcc Al. The values in parentheses for fcc Pt are or a sphere radius of $2.477a_0$ (a_0 being a Bohr radius) and for fcc Al are for a sphere radius of $2.557a_0$, while all the other values are for touching spheres. The lattice constants used in these calculations are $5.95a_0$, $7.4156a_0$, and $7.653a_0$ for bcc W, fcc Pt, and fcc Al, respectively. Note that for fcc Pt and Al with the full basis (double ζ+polarization), the total energy changes only by two-tenths of a millihartree due to a 5–7 % change in the sphere radius when the full-potential scheme is used. For the fcc and bcc cases we have used 110 and 70 special k points, respectively, in the irreducible wedge of the corresponding Brillouin zone.

	bcc W (hartrees)	fcc Pt (hartrees)	fcc Al (hartrees)
Single ζ muffin-tin	−16 156.5016	−18 436.2834	(−241.8778)
		(−18 436.2715)	
Full Potential	−16 156.5178	−18 436.2965	(−241.8818)
		(−18 436.2922)	
Double ζ+polarization muffin-tin	−16 156.5103	−18 436.2845	(−241.9156)
Full Potential	−16 156.5256	−18 436.3048	(−241.9195)
		(−18 436.3050)	−241.9193

IV. COHESIVE ENERGIES

The cohesive energy, which is defined as the difference in total energy between the solid state and the free atom, is more suitable for comparisons with other calculations and experiments. As can be seen from Table III, these agree quite well with other published calculations We would like to point out that our calculated cohesive energy with the full basis for bcc W agrees to a few hundredths of an eV with the FLAPW calculations of Refs. 4 and 5. This clearly shows that it is possible to achieve the accuracy of the FLAPW method with a much smaller local basis method.

The LDA result overestimates the (observed) cohesive energies and as one does a better job with the LDA, the discrepancy with the experiment grows. The problem here is believed[15] to be arising mainly from the atomic (LDA) calculations. For example the LDA predicts the wrong ground-state (d^5s) configuration for W.

The results listed in Table III involve the difference in calculated total energies for the solid and for the atom where, in both cases the valence shell was treated in the scalar-relativistic approximation and where a spin-polarized LDA calculation was done for the atom in the highest spin multiplicity appropriate to the atomic configuration. One of the problems is that the atomic LDA calculation involves an average over a set of spin multiplet levels. Spectroscopic data can be used to estimate the energy associated with promoting the atom from its ground state to this average. Accounting for this promotion reduces the calculated cohesive energies of Table III by 0.37 and 0.28 eV for W and Pt, respectively, reducing, but by no means removing, the discrepancy between the LDA theory and experiment. The exact discrepancy depends on the choice of the atomic configuration employed in the calculation. These issues will be explored in more detail in a future publication. It is to be emphasized that taking the differences in energies between different solids, as when calculating the heat of formation of a compound, meets with much greater numerical success. It is the inability of the LDA to deal with an atom with the same accuracy (or error) as the solid which adversely affects calculating a cohesive energy.

TABLE III. Cohesive energies for bcc W, fcc Pt, and fcc Al. Cohesive energies in eV for bcc W, fcc Pt, and Fcc Al calculated using the total energies of Table II (with the full basis) and spin-polarized atomic energies. These are shown together with results from other available calculations and experiments. The experimental values have been taken from Kittel (Ref. 11).

	bcc W (eV)	fcc Pt (eV)	fcc Al (eV)
Full-potential LASTO	9.77	7.11	3.98
Other theory	9.83[a]		3.64[d]
	9.76[b]		4.01[e]
	9.79[c]		
Experiment	8.90	5.84	3.39

[a]Reference 4.
[b]Reference 5.
[c]Reference 12.
[d]Reference 13.
[e]Reference 14.

CONCLUSIONS

We have discussed in detail our calculational method incorporating the full potential. There are two reasons for doing this. The first is to provide detailed explanations on the technically important, nontrivial points pertaining to these calculations, and the second is to give the reader an opportunity to compare our method with various other methods.[3–5,16,17] We have carried out fairly extensive tests on the numerical aspects of our method and have shown plots of the full potential and the density which may be used as checks for any future calculations. The plots showing the continuity of the potential (or the density) and its first derivative at the sphere boundaries and the various fine feature of these plots are not frequently reported in the literature. We have also reported on the sizes of these non-muffin-tin effects through various plots, band splittings, and total energies. Finally we have shown that this method is capable of yielding not only cohesive energies, but also total energies that compare very well with the all-electron FLAPW method.

ACKNOWLEDGMENTS

We thank Y.-J. Wang for doing the spin-polarized atomic calculations. This work was supported by the Division of Materials Sciences, Office of Basic Energy Sciences of the U.S. Department of Energy, under Contract No. DE-AC02-76CH00016, and by a grant of computer time at the National Magnetic Fusion Energy Computing Center (Livermore, California).

[1]J. W. Davenport, Phys. Rev. B **29**, 2896 (1984).
[2]J. W. Davenport, M. Weinert, and R. E. Watson, Phys. Rev. B **32**, 4876 (1985).
[3]E. Wimmer, H. Krakauer, M. Weinert, and A. J. Freeman, Phys. Rev. B **24**, 864 (1981).
[4]L. F. Mattheiss and D. R. Hamann, Phys. Rev. B **33**, 823 (1986).
[5]H. J. F. Jansen and A. J. Freeman, Phys. Rev. B **30**, 561 (1984).
[6]M. Weinert, J. Math. Phys. **22**, 2433 (1981).
[7]L. Hedin and B. I. Lundqvist, J. Phys. C **4**, 2064 (1971).
[8]D. Koelling, Rep. Prog. Phys. **41**, 139 (1981).
[9]M. Weinert, E. Wimmer, and A. J. Freeman, Phys. Rev. B **26**, 4571 (1982).
[10]G. W. Fernando, R. E. Watson, M. Weinert, and J. W. Davenport (unpublished).
[11]C. Kittel, *Introduction to Solid State Physics*, 5th ed. (Wiley, New York, 1976).
[12]C. T. Chan, D. Vanderbilt, S. G. Louie, and J. R. Chelikowski, Phys. Rev. B **33**, 7941 (1986).
[13]P. K. Lam and M. L. Cohen, Phys. Rev. B **24**, 4224 (1981).
[14]A. R. Williams, J. Kübler, and C. D. Gelatt, Phys. Rev. B **19**, 6094 (1979).
[15]V. L. Moruzzi, J. F. Janak, and A. R. Williams, *Calculated Electronic Properties of Metals* (Pergamon, New York, 1978).
[16]K. H. Weyrich, Phys. Rev. B **37**, 10 269 (1988).
[17]D. L. Price and B. R. Cooper, Phys. Rev. B **39**, 4945 (1989).